



# Unraveling the impact of Cu-doping in lead free halide perovskites for markedly enhancing photocatalytic CO<sub>2</sub> reduction performance

Naveen Kumar Tailor<sup>a,b,1</sup>, Shreya Singh<sup>d,1</sup>, Mohammad Adil Afroz<sup>a,b</sup>, Kamal Kishore Pant<sup>b,c,d,e,\*</sup>, Soumitra Satapathi<sup>a,b,\*\*</sup>

<sup>a</sup> Department of Physics, Indian Institute of Technology Roorkee, Roorkee 247667, India

<sup>b</sup> Center for Sustainable Energy, Indian Institute of Technology Roorkee, Roorkee 247667, India

<sup>c</sup> Department of Chemical Engineering, Indian Institute of Technology Roorkee, Roorkee 247667, India

<sup>d</sup> Catalytic Reaction Engineering Lab, Department of Chemical Engineering, Indian Institute of Technology Delhi, New Delhi 110016, India

<sup>e</sup> University of Saskatchewan, Saskatoon, SK S7N 5A2, Canada

## ARTICLE INFO

### Keywords:

CO<sub>2</sub> reduction

Photocatalyst

Perovskite

Lead free

Transient absorption spectroscopy

## ABSTRACT

Excessive CO<sub>2</sub> emissions from the consumption of fossil fuels contribute to both global warming and the energy crisis. To address these pressing issues, it is essential to capture and convert CO<sub>2</sub> into chemical feedstock using renewable energy such as solar energy. Solar-powered photocatalytic fuel production is widely acknowledged as a viable solution for a sustainable energy future. However, the development of high-performance photocatalysts remains a significant challenge to overcome in this endeavor. Recently, lead-free perovskites have emerged as a promising category of materials for CO<sub>2</sub> photoreduction, thanks to their remarkable optoelectronic properties, cost-effective solution processing, and non-toxic nature. Nonetheless, their inherent photocatalytic CO<sub>2</sub> reduction activity remains low due to the insufficient separation of photogenerated charges and the lack of active sites. Here, we demonstrate that Cu doping in lead-free double perovskites can lead to markedly enhanced CO<sub>2</sub> reduction performance. The interstitial Cu dopants modulate the fermi level and introduce the active energy sites near the conduction band, which significantly enhances light absorption and separation of charge carriers. The Cu-Cs<sub>2</sub>AgBiCl<sub>6</sub> shows the activity of 88 and 48 μmol/g<sub>cat</sub> for CH<sub>4</sub> and CO products which are both higher than those of the pristine Cs<sub>2</sub>AgBiCl<sub>6</sub> (27 and 10 μmol/g<sub>cat</sub>). The total yield of Cu-Cs<sub>2</sub>AgBiCl<sub>6</sub> perovskite for CO<sub>2</sub> photoreduction is superior to those reported under similar conditions. Transient absorption results show that hot carrier relaxation is slower and carrier decay lifetime is extended in Cu-Cs<sub>2</sub>AgBiCl<sub>6</sub>, which can enhance the charge migration efficiency and boost the CO<sub>2</sub> reduction performance. These findings provide valuable insight into the mechanism of CO<sub>2</sub> reduction in Cu-doped Cs<sub>2</sub>AgBiCl<sub>6</sub> perovskite crystals and suggest that Cu-doping is a promising strategy for developing highly efficient and selective CO<sub>2</sub> reduction photocatalysts.

## 1. Introduction

The emission of greenhouse gases, notably carbon dioxide (CO<sub>2</sub>), into the atmosphere leads to global warming, rise in sea levels, and the increasing frequency of natural disasters. Researchers have proposed a variety of strategies to mitigate the negative effects of CO<sub>2</sub> emissions and climate change, including the development of CO<sub>2</sub> capture technologies and the conversion of CO<sub>2</sub> into value-added chemical fuels such as CO, CH<sub>4</sub>, CH<sub>3</sub>OH, etc [1–4]. Although converting CO<sub>2</sub> into fuel poses

significant scientific challenges, it has enormous potential for mitigating global warming and generating renewable energy. Photocatalytic CO<sub>2</sub> reduction, first reported by Inoue et al. in 1979, has been demonstrated in aqueous solutions using various semiconductor photocatalysts [5]. Since then, scientists have developed nanostructured materials, such as metal oxide, metal sulfide, and halide perovskites, for this purpose [6–15]. Due to their high carrier mobility, long diffusion duration, and tunable light absorption property, metal halide hybrid perovskites have recently been identified as a promising candidate for photocatalytic CO<sub>2</sub>

\* Corresponding author at: Center for Sustainable Energy, Indian Institute of Technology Roorkee, Roorkee 247667, India.

\*\* Corresponding author at: Department of Physics, Indian Institute of Technology Roorkee, Roorkee 247667, India.

E-mail addresses: [dr.kkpant@gmail.com](mailto:dr.kkpant@gmail.com) (K.K. Pant), [soumitra.satapathi@ph.iitr.ac.in](mailto:soumitra.satapathi@ph.iitr.ac.in) (S. Satapathi).

<sup>1</sup> Both authors contributed equally to this work.

reduction [11,12,16,17]. For instance, Kong et al. demonstrated that the in-situ growth of a metal-organic framework on the surface of CsPbBr<sub>3</sub> quantum dots can substantially enhance the photocatalytic capability for CO<sub>2</sub> reduction [18]. In another study, Xu et al. achieved higher efficiency in CO<sub>2</sub> photochemical conversion by combining CsPbBr<sub>3</sub> quantum dots with graphene oxide [19]. However, the lead toxicity and poor environmental stability of these halide perovskite materials require the development of lead-free perovskite materials with comparable optoelectronic properties. In this regard, lead-free Bismuth halide lead-free perovskites have emerged as a promising class of optoelectronic materials due to their nontoxicity and rich structural diversity [20–28]. Our group previously reported the fundamental characteristics and optoelectronic properties of bismuth halide perovskites [20,29–33]. Moreover, these materials have been applied for CO<sub>2</sub> reduction by several research groups. Wu et al. showed that halide engineering can boost the CO<sub>2</sub> photoreduction of bismuth halide nanocrystals [34]. Pi et al. observed that the chlorine vacancy plays a triple role in this process: it suppresses photogenerated electron-hole recombination, enhances CO<sub>2</sub> adsorption, and significantly reduces the free energy barrier for the generation of the key intermediate COOH\* [35]. By coupling the surface and defect engineering of the hierarchical Cs<sub>2</sub>NaBiCl<sub>6</sub> sample, they were able to achieve a remarkable 12.34-fold enhancement of CO<sub>2</sub> photoreduction activity. Sena et al. showed that a composite of Cs<sub>2</sub>AgBiBr<sub>6</sub> on a 2D bismuthene nanosheet led to enhanced photocatalytic activity [36]. This increased photocatalytic activity was ascribed to the perovskite and bismuthene's strong interfacial contact, which resulted in enhanced charge separation and decreased electron-hole recombination. Despite these advancements, significant challenges remain in the application of bismuth halide perovskites for CO<sub>2</sub> reduction. The performance of pristine perovskites in terms of CO<sub>2</sub> adsorption and activation remains unsatisfactory due to their inherent limitations in effectively capturing and activating CO<sub>2</sub> molecules. Additionally, photogenerated holes and electrons may tend to recombine rather than take part in the catalytic process due to the low carrier separation efficiency and short lifetime. These challenges need to be addressed to further improve the CO<sub>2</sub> reduction potential of bismuth halide perovskites.

To mitigate the challenges in the application of bismuth halide perovskites for CO<sub>2</sub> reduction, various strategies have been proposed. One such strategy is the creation of heterojunctions with materials such as Bi<sub>2</sub>WO<sub>6</sub> [28], r-GO [37], and carbon nitrides [38], which promote carrier separation. While another strategy is doping with metal ions, which can modulate the energy band structure, enhance light absorption, act as electron capture centers, provide photocatalytic sites, and promote the separation of photogenerated electron-hole pairs [39]. In this work, we focus on the latter strategy and investigate the impact of Cu-doping on the CO<sub>2</sub> reduction performance of the bismuth halide double perovskite Cs<sub>2</sub>AgBiCl<sub>6</sub>. We have selected double perovskites due to their three-dimensional crystal structure, which distinguishes them from the A<sub>3</sub>Bi<sub>2</sub>X<sub>9</sub> bismuth-halide perovskites (a vacancy ordered perovskite). Double perovskites, as previously discussed by Shi et al., exhibit lower exciton binding energy and effective carrier mass, along with higher carrier mobility and lifetime. These advantageous characteristics make double perovskites superior to other low-dimensional perovskite materials [40].

In this direction, various strategies have been proposed to enhance the CO<sub>2</sub> photoreduction performance of these materials. Surface modification with noble metals, rGO, etc., is a feasible method to promote carrier separation efficiency [25,41]. Heterojunction construction with Bi<sub>2</sub>WO<sub>6</sub>, carbon nitride, and other perovskites is also an effective means of promoting carrier separation [26–28,42]. Doping with metal ions is a convenient method of enhancing the catalytic performance of photocatalysts [43–45]. Dopants play a crucial role in modifying the energy band structure of semiconductor materials. They facilitate light absorption, serve as electron capture centers, create additional photocatalytic sites on the material surface, and promote the efficient separation of photogenerated electron-hole pairs [39,46]. Certain

dopants can serve as specific catalytic sites for adsorbing target substrates and improving corresponding catalytic activity. For instance, experimental and theoretical evidence has shown that doping the CsPbBr<sub>3</sub> catalyst with various transition metals improves its CO<sub>2</sub> reduction efficiency. However, the detailed effects of dopants on CO<sub>2</sub> activation mechanisms and carrier dynamics in bismuth halide perovskites have received limited attention and require further investigation. The effect of dopants on excited state dynamics and carrier relaxation process, and how it affects CO<sub>2</sub> reduction performance, is yet to be thoroughly explored. Therefore, gaining a profound and comprehensive understanding of these effects is fundamental and indispensable for the development of efficient perovskite catalysts.

In this study, we have explored the catalytic potential of Cs<sub>2</sub>AgBiCl<sub>6</sub>, a bismuth halide double perovskite, for CO<sub>2</sub> reduction and examined the impact of Copper (Cu) doping on its performance. Copper, an environmentally friendly and economical transition metal, is well known for its catalytic ability. The Cs<sub>2</sub>AgBiCl<sub>6</sub> perovskite crystals with and without Cu-doping were grown via a slow cooling method. Notably, the incorporation of Cu into the Cs<sub>2</sub>AgBiCl<sub>6</sub> lattice markedly improved the absorption region. EDXA and XPS spectra confirm the presence of Cu in Cs<sub>2</sub>AgBiCl<sub>6</sub>. UPS spectra reveal that Cu-doping alters the fermi levels in the semiconductor and increment in the n-type characteristics in Cs<sub>2</sub>AgBiCl<sub>6</sub>. The enhanced CO<sub>2</sub> reduction activity was attributed to the increased charge carrier separation and migration efficiency, as well as the introduction of Cu active sites that facilitate the CO<sub>2</sub> reduction reaction. Transient absorption measurement shows that hot carrier relaxation is slower and the carrier decay time is extended in the Cu-Cs<sub>2</sub>AgBiCl<sub>6</sub>, which significantly boosts the CO<sub>2</sub> reduction performance. Our results provide valuable insights into the CO<sub>2</sub> reduction performance and mechanism of Cu-doped Cs<sub>2</sub>AgBiCl<sub>6</sub> perovskite crystals. These findings provide valuable insights into the CO<sub>2</sub> reduction performance and mechanism of Cu-doped Cs<sub>2</sub>AgBiCl<sub>6</sub> perovskite crystals and could facilitate the rational design and development of efficient and selective CO<sub>2</sub> reduction photocatalysts based on halide perovskite crystals.

## 2. Experimental section

### 2.1. Chemicals

Cesium(I) chloride (CsCl, Sigma Aldrich, 99%), silver(I) chloride (AgCl, Sigma Aldrich, 99.99%), bismuth (III) chloride (BiCl<sub>3</sub>, Sigma Aldrich 99%), and copper (I) chloride (CuCl, TCI Chemicals) were used as received. Hydrochloric acid (HCl 35–38%) was purchased from s d fine-CHEM limited (SDFCL).

### 2.2. Synthesis of Cs<sub>2</sub>AgBiCl<sub>6</sub> and Cu-Cs<sub>2</sub>AgBiCl<sub>6</sub> single crystals

To initiate crystal growth, a solution was prepared at room temperature by dissolving 2.0 mmol of CsCl and 1.0 mmol of BiCl<sub>3</sub> in HCl. AgCl was then added, and the solution was briefly stirred. The vial containing the solution was then heated to 120 °C and held at this temperature until the solution became clear and transparent. Subsequently, the solution was cooled at a controlled rate of 0.3 °C per hour, and the temperature was maintained overnight to facilitate crystal growth. This process typically takes 8 days to complete. Cu-Cs<sub>2</sub>AgBiCl<sub>6</sub> crystals were grown with a similar process adding the Cu(I)Cl in the precursor solution. The as-grown crystals were handled with care and washed with chlorobenzene to remove any residual chemicals from their surfaces.

### 2.3. Characterizations

The photograph of crystals was captured using a DSLR camera. Powder X-ray diffraction datasets were collected using a Bruker (D8-Advance Model) diffractometer equipped with a LINXEYE XE detector and Cu-K $\alpha$  radiation ( $\lambda = 1.54 \text{ \AA}$ ). ICPMS were performed using the 8900

ICP-MS Triple Quad (Agilent) instrument in diluted liquid samples. The ultraviolet-visible (UV-vis) absorption spectra of the single-crystals were measured using a Microprocessor UV-Vis Double Beam spectrophotometer Cary 100 with an attached integrating sphere for measurement of diffused reflectance. For the Raman spectra measurement, the WITec alpha300 RA Raman instrument was used with a laser source of 532 nm. ESR spectra of all single crystals were measured by BRUKER BIOSPIN, Germany Model- EMXmicro A200–9.5/12/S/W Microwave X Band source. The magnetic field was applied in the range of 1000 Gauss to 6000 Gauss. A microwave frequency of 9.4 GHz was used. X-ray photoelectron spectroscopy (XPS) and Ultraviolet photoelectron spectroscopy (UPS) were performed using PHI 5000 Versa Probe III instrument.

## 2.4. Methodology for CO<sub>2</sub> photoreduction

5 mg of the photocatalyst material was dispersed in 5 mL anhydrous iso-propyl-alcohol (IPA) and was then spread onto the bottom of a stainless-steel reactor of length 125 mm and diameter 90 mm with quartz top for illumination, with the total internal volume being 350 mL. N<sub>2</sub> gas was purged into the reactor to ensure that the system is free from carbon-based impurities. CO<sub>2</sub> (99.99%) was then purged into the photoreactor at 25 mL min<sup>−1</sup> for 15 min. The reactor was then closed with an internal pressure maintained at 1.5 atm, and temperature kept at room temperature. Mercury halogen lamp (250 W) served as the illumination source, which was maintained at 20 °C using the cooling arrangements. After 4 h of reaction, the gas samples were collected and analyzed with a gas chromatograph (CS5800, Centurion Scientific) equipped with a packed column (Hayesep-A, length 2 m, diameter 2.1 mm; Molsieve 5 A, 15 m × 0.25 mm). Both flame-ionization detector (FID) and thermal conductivity detector (TCD) with methanizer connected in the switching arrangement were used to analyze the reaction products, with inlet temperature being 170 °C and oven held at 70 °C for 4 min then raised to 160 °C. The argon (99.99%) served as a carrier gas at a flow rate of 3 mL min<sup>−1</sup>. The recyclability of the Cu-Cs<sub>2</sub>AgBiCl<sub>6</sub> material was assessed through a cyclic experiment, employing the identical photocatalyst used in the earlier activity test run. The catalyst preparation involved evaporating the solvent from its suspension with the catalyst, then thoroughly drying it overnight at 120 °C within a hot air oven. The performance test was initiated by subjecting the catalyst to the CO<sub>2</sub> photoreduction procedure as described above. After each reaction cycle, the catalyst was gathered, purified, and re-dried using the preliminary method, thereby priming it for the subsequent cycle. This test spanned across three full cycles, whereupon the CO and CH<sub>4</sub> formation rates were compared after each one.

## 2.5. Computational details

The first-principles calculations were performed using the DMOL<sup>3</sup> code, based on density functional theory (DFT) performed in Materials Studio 20.1 (Biovia, San Diego) software. Electron-ion interaction was treated using the ultrasoft pseudopotential (USP) method, while the exchange interaction of electrons was considered using the generalized gradient approximation proposed by Perdew–Burke–Ernzerhof (GGA-PBE). Geometry optimization was carried out before the single-point energy calculation, and the self-consistent energy convergence accuracy was set to 1.0e-4 Ha. The convergence criteria for the self-consistent field (SCF) density were defined as 1.0e-4 Ha for energy, 0.02 Ha/Å for force, and 0.05 Å for atom displacements. These criteria were applied within the Monkhorst–Pack k-point mesh of dimensions 3 × 3 × 1.

## 3. Results and discussion

### 3.1. Structural and elemental characterization

We utilized single crystal powders as the catalysts for CO<sub>2</sub> reduction

due to their higher specific surface area compared to directly synthesized powders. Moreover, single crystals exhibit significantly higher phase purity than polycrystalline thin films [47–49]. To obtain these single crystals, Cs<sub>2</sub>AgBiCl<sub>6</sub> and Cu-Cs<sub>2</sub>AgBiCl<sub>6</sub> were grown using the slow cooling method, and the experimental details are provided in the experimental section. The resulting millimeter-sized single crystals are depicted in Fig. 1a, appearing as truncated octahedrons. Furthermore, elemental analysis confirmed the Cu-doping of the Cs<sub>2</sub>AgBiCl<sub>6</sub> crystal (Fig. S1 and S2; Table S1 and S2). The weight % and atomic % of Cu were found as 1.3% and 1.7%, respectively (Fig. 1b). ICPMs results also show the Cu doping in Cs<sub>2</sub>AgBiCl<sub>6</sub> (Table S3). The double perovskites possess a three-dimensional structure composed of corner-connected octahedra, with cuboctahedral cavities in the framework occupied by Cs<sup>+</sup> ions. The rock salt ordering is formed by alternating Ag<sup>+</sup> and Bi<sup>3+</sup> centered octahedra in all directions. In a Cs<sub>2</sub>AgBiCl<sub>6</sub> double perovskite, cuboctahedra contain a Cs<sup>+</sup> ion at the center, surrounded by alternating [BiCl<sub>6</sub>]<sup>−3</sup> and [AgCl<sub>6</sub>]<sup>−5</sup> octahedral units (Fig. 1e) [24,31].

To observe the effect of Cu-doping on the crystal structure, we performed the XRD experiment. In the XRD pattern, the main peaks for Cs<sub>2</sub>AgBiCl<sub>6</sub> are observed at 2θ = 14.58° (111), 29.01° (222), 43.92° (333), and 59.61° (444) (Fig. 1c). The obtained diffraction pattern matches well with the reference pattern of Cs<sub>2</sub>AgBiCl<sub>6</sub> in the database (ICSD collection #239874). The Cs<sub>2</sub>AgBiCl<sub>6</sub> possesses a cubic crystal structure with a centrosymmetric *Fm-3m* space group [24]. The XRD pattern of Cu-Cs<sub>2</sub>AgBiCl<sub>6</sub> confirms the retention of the perovskite host structure after Cu-doping. However, the peak positions in Cu-Cs<sub>2</sub>AgBiCl<sub>6</sub> shift towards lower diffraction angles, indicating an increase in the lattice spacing (Fig. 1d). Powder XRD of both samples reveals a shift in all peaks towards lower diffraction angles in Cu-Cs<sub>2</sub>AgBiCl<sub>6</sub>, indicating lattice expansion (Fig. S3). Previous studies have shown that XRD patterns of interstitial dopants exhibit a negative shift, while substitution dopants show a positive shift [39,50]. Considering the smaller ionic radius of Cu<sup>+</sup> (~77 pm) compared to Bi<sup>3+</sup> (≈ 103 pm) and Ag<sup>+</sup> (126 pm), the introduced Cu ions were assumed to be interstitial dopants in the [BiCl<sub>6</sub>]<sup>−3</sup> and [AgCl<sub>6</sub>]<sup>−5</sup> octahedral units. Therefore, it can be concluded that the introduced Cu ions are interstitial dopants in the bulk Cs<sub>2</sub>AgBiCl<sub>6</sub> catalyst. The lattice parameters of Cs<sub>2</sub>AgBiCl<sub>6</sub> and Cu-Cs<sub>2</sub>AgBiCl<sub>6</sub> are estimated to be a = b = c = 10.74 Å and a = b = c = 10.78 Å, respectively. The volume of unit cells is increased in the case of Cu-Cs<sub>2</sub>AgBiCl<sub>6</sub> (1253.55 Å<sup>3</sup>) than the Cs<sub>2</sub>AgBiCl<sub>6</sub> (1239.24 Å<sup>3</sup>). Due to the disparity in ionic sizes and valence states between Cu<sup>+</sup> ions and host lattice ions, a strain is induced on the lattice, consequently impacting the size and volume of the unit cell. Previously it was reported that doping can reduce the defect density and lattice strain, which enhances the diffusion length and reduce charge carrier recombination in perovskite devices [46,51]. In our case, we find that FWHM of prominent plane peaks reduces and crystallite size increases with Cu doping (Fig. S4, Table S4-S7). The lattice strain of all planes reduces with Cu-doping, which might be attributed to relaxation by the generation of dislocations. Additionally, the interstitial doping strategy has been reported to effectively suppress ion migration within metal halide perovskites [50]. This doping approach enables efficient neutralization of negatively charged defects within the crystals, enhancing charge separation, and improving the efficiency of charge collection.

We did XPS to perform a quantitative analysis of the electronic structures and chemical properties of Cu-Cs<sub>2</sub>AgBiCl<sub>6</sub> double perovskite. Fitted XPS spectra are shown in Fig. S5 and S6. Fig. 2a shows the narrow XPS spectra of 3d-Cs, revealing two strong peaks at 724.03 eV and 738.15 eV attributed to 3d<sub>5/2</sub>-Cs and 3d<sub>3/2</sub>-Cs, respectively, in agreement with the standard Cs element. The two peaks were separated by an energy value of 14.12 eV. The 3d-Ag spectra exhibited two peaks at 367.57 and 373.63 eV associated with Ag 3d<sub>5/2</sub> and Ag 3d<sub>3/2</sub>, respectively (Fig. 2b). The Bi core-level peaks were detected at binding energies of 159.05 eV (Bi 4f<sub>7/2</sub>) and 164.5 eV (Bi 4f<sub>5/2</sub>) with an energy separation of 5.45 eV, indicative of the Bi<sup>3+</sup> species (Fig. 2c). In Fig. 2d, the Cl 2p spectra displayed two peaks at 197.92 and 199.43 eV

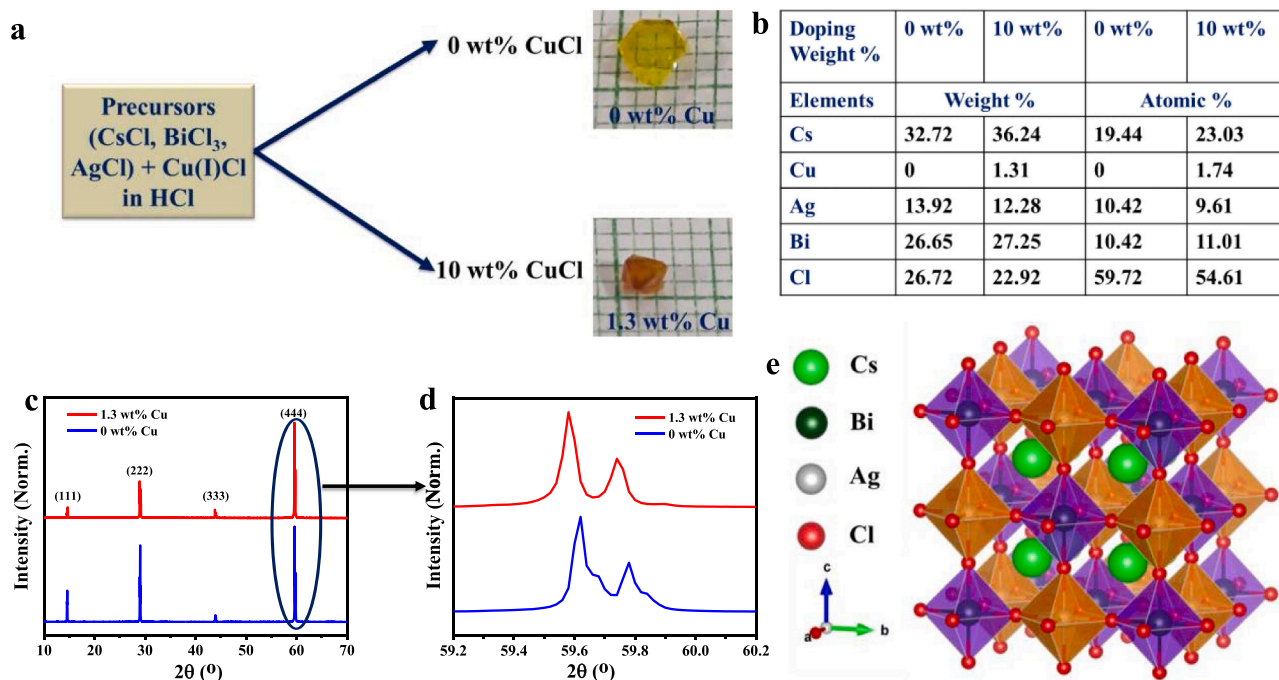


**Fig. 1.** (a) The photograph of as-grown Cs<sub>2</sub>AgBiCl<sub>6</sub> and Cu-Cs<sub>2</sub>AgBiCl<sub>6</sub> single crystals. (b) The elemental analysis for these systems. (c) X-ray diffraction pattern, (d) Expansion of Fig. c to show 444 peak of XRD (e) Crystal structure of Cs<sub>2</sub>AgBiCl<sub>6</sub>.

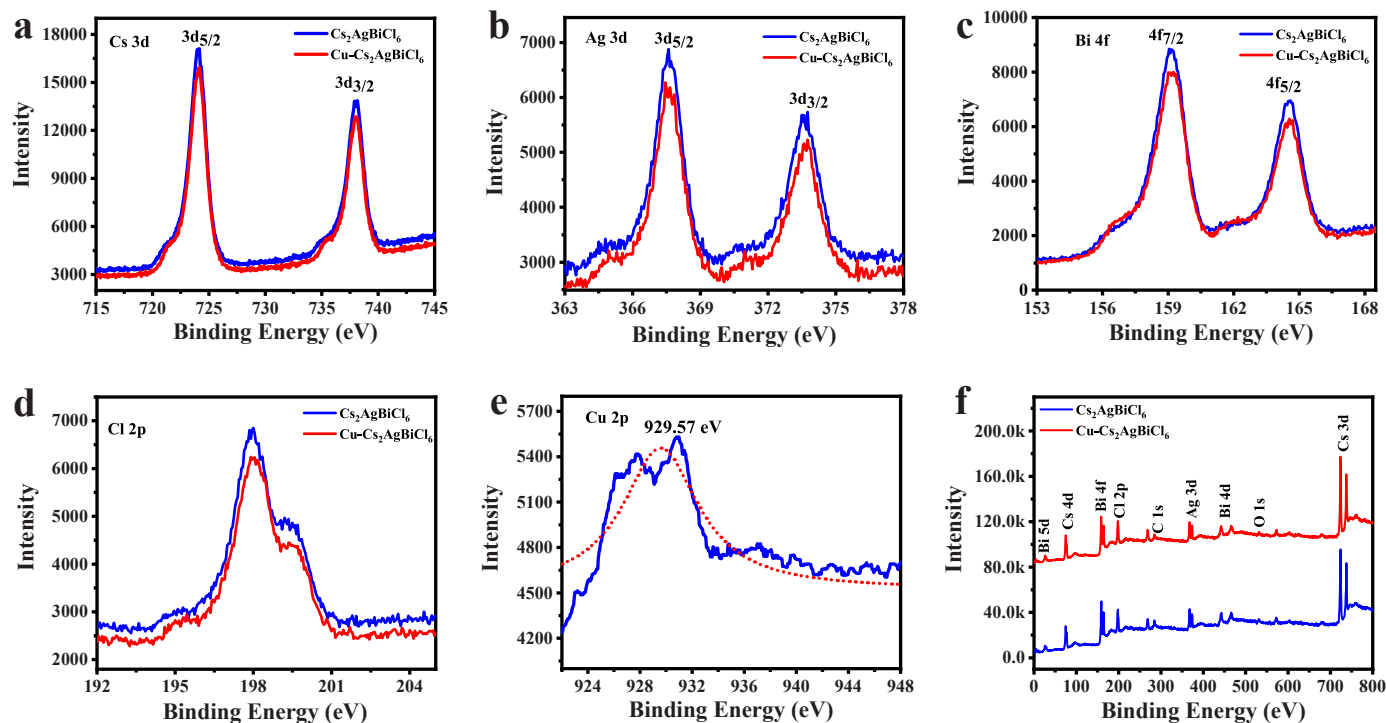


**Fig. 2.** XPS spectra of Cs<sub>2</sub>AgBiCl<sub>6</sub> and Cu-Cs<sub>2</sub>AgBiCl<sub>6</sub> crystals. (a) Cs 3d, (b) Ag 3d, (c) Bi 4 f, (d) Cl 2p for Cs<sub>2</sub>AgBiCl<sub>6</sub> crystals. (e) XPS spectra of Cu 2p crystal. (f) Survey spectrum of Cs<sub>2</sub>AgBiCl<sub>6</sub> and Cu-Cs<sub>2</sub>AgBiCl<sub>6</sub> systems.

corresponding to Cl 2p<sub>3/2</sub> and Cl 2p<sub>1/2</sub>, respectively. The intensity of the corresponding energy spectral peaks decreased after the addition of Cu leading to different chemical environments around Bi, Ag, and Cs upon Cu incorporation. However, the peak positions remained almost unchanged. A weak Cu 2p<sub>3/2</sub> signal at 929.57 eV was observed, indicating that copper (Cu) is present in the doped crystals as Cu<sup>+</sup> ions (Fig. 2e) [52]. This finding aligns with previous reports, as the core levels of Cs

3d, Ag 3d, Bi 4 f, and Cl 2p in the full XPS spectra remain consistent (Fig. 2f) [53–56]. The presence of interstitial Cu dopants leads to interactions with the surrounding Bi, Ag, and Cl atoms, which may affect the adsorption or activation of CO<sub>2</sub> molecules on the surface of Cu-Cs<sub>2</sub>AgBiCl<sub>6</sub> catalysts.



### 3.2. Spin and optical characterization

The magnitude of the ESR signal is directly related to the concentration of ESR active species present in the material. Electron spin relaxation typically determines the EPR linewidth. At room temperature, the ESR signal in  $\text{Cs}_2\text{AgBiCl}_6$  is very low. However, the intensity of the EPR signals increases in  $\text{Cu-Cs}_2\text{AgBiCl}_6$  (Fig. 3a, S7), which confirms that spin active sites are enhanced after doping [44]. Moreover, negligible change was observed in the width of the EPR signal, which indicates that the spin-spin relaxation time remains unchanged with the Cu-doping. In  $\text{Cu-Cs}_2\text{AgBiCl}_6$ , the  $g$ -value is slightly shifted compared to that of  $\text{Cs}_2\text{AgBiCl}_6$  (Fig. 3b). The shift in the  $g$ -value can be attributed to enhanced spin-orbit coupling due to increased spin-active sites in  $\text{Cu-Cs}_2\text{AgBiCl}_6$ . Further, the Raman spectra was measured using a 532 nm excitation source. The Raman peaks observed in the  $\text{Cs}_2\text{AgBiCl}_6$  crystal were located at 74.3, 118.7, 220.1, and 286.6  $\text{cm}^{-1}$  (Fig. 3c). The bending frequency of  $\delta(\text{Cl-Ag-Cl})$  and  $\delta(\text{Cl-Bi-Cl})$  are responsible for the mode at 74.3  $\text{cm}^{-1}$ . The band observed at 118.7  $\text{cm}^{-1}$  can be attributed to the breathing vibration of Ag-Cl bonds exhibiting  $T_{2g}$  symmetry. Furthermore, the stretching vibrations of the  $\text{AgCl}_6$  octahedron, displaying distinct vibrational symmetries of  $E_g$  and  $A_{1g}$ , are responsible for the two bands at 220.1 and 286.6  $\text{cm}^{-1}$ , respectively. We observed slight peak position shifts with Cu doping due to the local environment of Cu dopants and their interaction with the halide ions in the crystal [57–59].

The steady-state absorption spectrum of  $\text{Cu-Cs}_2\text{AgBiCl}_6$  SC exhibits an absorption edge of approximately 700 nm, which is extended by approximately 210 nm compared to that of the pristine  $\text{Cs}_2\text{AgBiCl}_6$  crystal (Fig. 3d). This increase in absorption can be attributed to defects introduced by Cu doping (d-d transition of Cu) [60,61]. The Urbach energy was estimated as 68.54 meV and 239.34 meV for the  $\text{Cs}_2\text{AgBiCl}_6$  and  $\text{Cu-Cs}_2\text{AgBiCl}_6$ , respectively (Fig. 3e). The increase in Urbach energy for the  $\text{Cu-Cs}_2\text{AgBiCl}_6$  perovskite can be attributed to the formation of Cu-related defects, which can introduce local disorder into the crystal lattice. The increase in Urbach energy also leads to the broadening of the absorption spectrum, which can affect the efficiency of the material for

photocatalytic  $\text{CO}_2$  reduction. Furthermore, we calculated the indirect bandgap using Tauc plot, and the bandgap was found to be 2.55 eV for the  $\text{Cs}_2\text{AgBiCl}_6$  crystal. According to the Tauc plot calculation, we found that the bandgap of  $\text{Cu-Cs}_2\text{AgBiCl}_6$  did not change significantly; instead, defect states were introduced after Cu doping, resulting in an additional tail (Fig. 3f) [61,62]. The observed extended absorption in the  $\text{Cu-Cs}_2\text{AgBiCl}_6$  can be attributed to the induced defect states. The cubic crystal structure and close packing were not affected by Cu doping, but the alteration of  $[\text{AgCl}_6]^{-5}$  and  $[\text{BiCl}_6]^{-3}$  octahedrons can cause crystal distortion and movement of energy levels.

### 3.3. Energy level measurement

Moreover, we used ultraviolet photoelectron spectroscopy (UPS) to determine the Fermi level ( $E_F$ ), valence band maximum (VBM), and conduction band minimum (CBM) as shown in Fig. 4a and.

**4b.** The binding energy of  $\text{Cs}_2\text{AgBiCl}_6$  was estimated as 1.14 eV with a cutoff energy of 16.05 eV, which allowed us to estimate the VBM,  $E_F$ , and CBM of  $\text{Cs}_2\text{AgBiCl}_6$  to be  $-6.3$ ,  $-5.16$ , and  $-3.75$  eV, respectively (Fig. S8a). Based on the position of the Fermi level, we determined that pristine  $\text{Cs}_2\text{AgBiCl}_6$  exhibited  $p$ -type semiconductor behavior. For  $\text{Cu-Cs}_2\text{AgBiCl}_6$ , we measured a binding energy of 1.70 eV and cutoff energy of 16.27 eV. Using this data, we estimated the VBM,  $E_F$ , and CBM of  $\text{Cu-Cs}_2\text{AgBiCl}_6$  to be  $-6.64$ ,  $-4.94$ , and  $-4.09$  eV, respectively (Fig. S8b). We observed that the Fermi level had shifted near the CBM in  $\text{Cu-Cs}_2\text{AgBiCl}_6$ , resulting in  $n$ -type semiconductor behavior [63–65]. Both VBM and CBM levels shifted towards more negative values in Cu-doped samples. In the  $\text{Cs}_2\text{AgBiCl}_6$ , CBM and VBM are located at  $-1.10$  eV and  $1.45$  eV vs. NHE positions, respectively. In the  $\text{Cu-Cs}_2\text{AgBiCl}_6$ , CBM and VBM are located at  $-0.76$  eV and  $1.79$  eV vs. NHE positions, respectively (Fig. 4c). This potential is thermodynamically sufficient for the reduction of  $\text{CO}_2$  to CO and  $\text{CH}_4$  [16,66,67].

### 3.4. $\text{CO}_2$ photoreduction performance evaluation

Further, we tested the  $\text{CO}_2$  photoreduction performance and

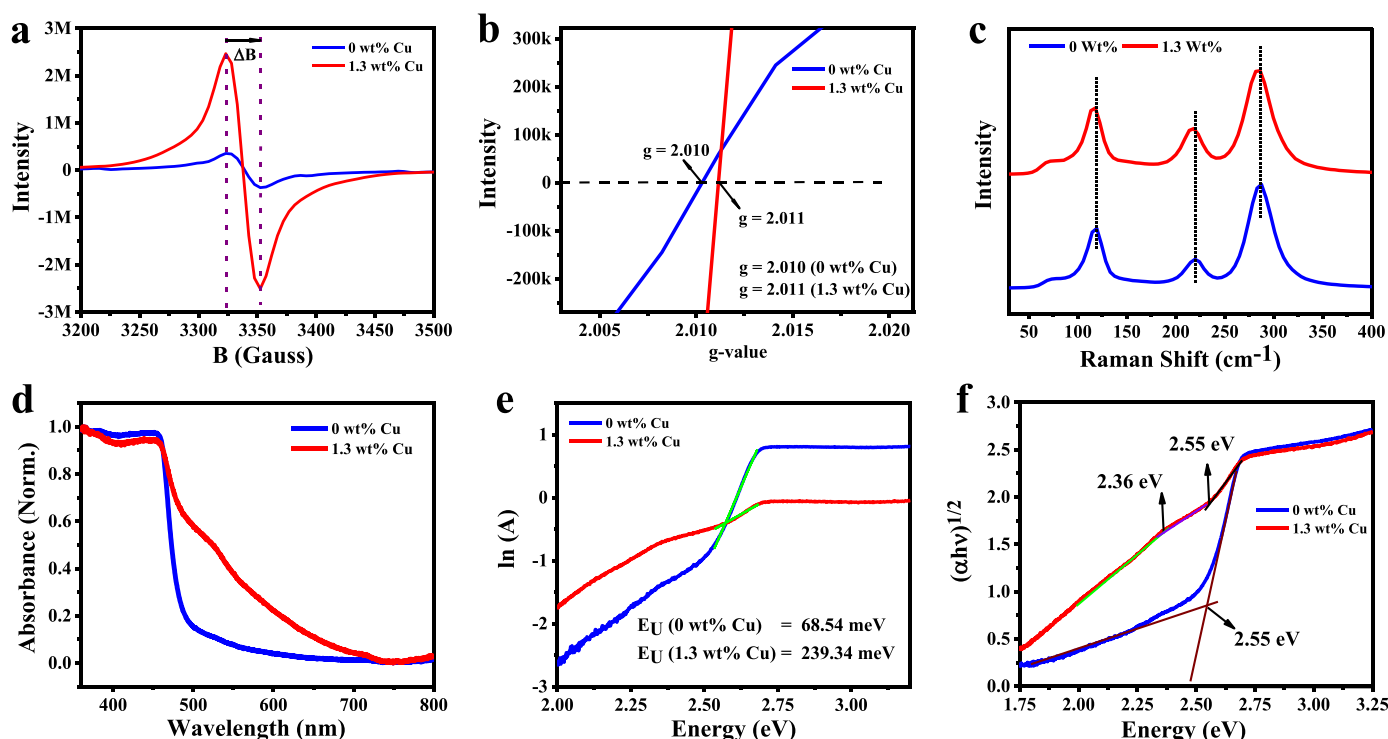
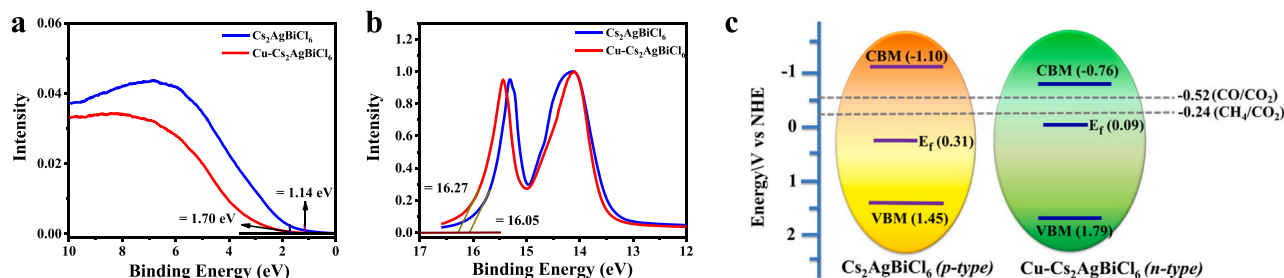


Fig. 3. (a) ESR Spectra, (b)  $g$ -value, (c) Raman spectra, (d) Absorption spectra, (e) Urbach energy, (f) bandgap of  $\text{Cs}_2\text{AgBiCl}_6$  and  $\text{Cu-Cs}_2\text{AgBiCl}_6$ .



**Fig. 4.** (a) UPS valence band edge region (b) UPS cut-off region for both  $\text{Cs}_2\text{AgBiCl}_6$  and  $\text{Cu-Cs}_2\text{AgBiCl}_6$  system. (c) Schematic illustration of the band positions and Fermi levels.

observed the formation of CO and  $\text{CH}_4$  as the reduced products. No traces of  $\text{H}_2$  or any other gases were observed, thus illustrating a high catalyst selectivity for  $\text{CO}_2$  photoreduction. Figs. 5a and 5b demonstrate the photoreduction performance of  $\text{Cs}_2\text{AgBiCl}_6$  and  $\text{Cu-Cs}_2\text{AgBiCl}_6$  in terms of the generation rates of  $\text{CH}_4$  and CO after the reaction. The introduction of copper into the  $\text{Cs}_2\text{AgBiCl}_6$  matrix leads to significant variations in the photocatalytic performance, particularly an increase in the photoreduction yield from 27 and 10  $\mu\text{mol/g}_{\text{cat}}$  to 88 and 48  $\mu\text{mol/g}_{\text{cat}}$  for  $\text{CH}_4$  and CO products, respectively. While there was a slight decrease in selectivity towards  $\text{CH}_4$  production, from 72% to 65%, on  $\text{Cu-Cs}_2\text{AgBiCl}_6$ , the selectivity for CO increased from 28% to 35%. Importantly, despite these changes in selectivity, the total product yield from the  $\text{Cu-Cs}_2\text{AgBiCl}_6$  catalyst was significantly higher compared to that from the  $\text{Cs}_2\text{AgBiCl}_6$  catalyst. In addition, the total yield of  $\text{Cu-Cs}_2\text{AgBiCl}_6$  perovskite for  $\text{CO}_2$  photoreduction is superior to those reported under similar conditions (as shown in Table S8) for other halide perovskite materials. We also evaluated the catalytic ability of the well-recognized lead perovskite material,  $\text{CsPbBr}_3$ , under similar conditions for comparison (Table S8). Significantly, the catalytic performance of  $\text{Cu-Cs}_2\text{AgBiCl}_6$  was although low but comparable to that of  $\text{CsPbBr}_3$ , with the added advantage of being lead-free and thus environmentally benign. The non-toxic nature of  $\text{Cu-Cs}_2\text{AgBiCl}_6$  positions it as a promising catalyst for green  $\text{CO}_2$  conversion, combining efficacy with environmental safety. Based on previous literature as well as our findings, it can be well corroborated that  $\text{Cs}_2\text{AgBiCl}_6$  has appropriate band edges positioned to perform the  $\text{CO}_2$  photoreduction. The enhancement in the production rates can be attributed to the incorporation of Cu in the crystal structure of  $\text{Cs}_2\text{AgBiCl}_6$  perovskites which led to the red shift in the absorbance spectra and increased Urbach energy which can be ascribed to the increment in the structural defects, thus enlarging the optical absorbance and electron transportation on light excitation that can be utilized in the  $\text{CO}_2$  conversion process.

The ease of electron transport is improved significantly on the incorporation of Cu into the crystal of halide perovskite material, which

can be observed from the changing value of  $E_f$  for pristine and Cu incorporated materials (Fig. 4c). The reduced work function values demonstrate the enhanced feasibility of electron transfer to reduce the surface adsorbed  $\text{CO}_2$  to generate  $\text{CH}_4$  and CO. The presence of structural defects and electron transportation ability due to the presence of copper centers greatly influenced the reduction ability of the photocatalyst material indicating a more robust reduction tendency of the photogenerated electrons due to copper. Fig. S9 shows the  $\text{CO}_2$  temperature programmed desorption profile for  $\text{Cu-Cs}_2\text{AgBiCl}_6$  material, strong peak positioned in the region 250–450°C indicates a more concentration of the moderate basic sites compared to weak (50–250°C) and strong basic sites (450–600°C) which is desired for the  $\text{CO}_2$  activation and reduction tendency. Further, the electronic transition mechanism is investigated using transient absorption spectroscopy and is discussed in the later section. To provide additional evidence for the origin of the detected gas products, we have conducted control experiments including the absence of light,  $\text{CO}_2$  and using labelled  $^{13}\text{C}$ . These experiments were employed to confirm that the CO and  $\text{CH}_4$  products were indeed derived from the photocatalytic reduction of  $\text{CO}_2$  over the photocatalyst material. No significant product formation was observed for the experiments conducted in the absence of light and  $\text{CO}_2$ . Also, the peaks observed at  $m/z$  17 and 29 (Fig. 5A inset) confirm the primary carbon source in the reduction experiment. These results affirm that the observed gas products primarily originated from the reduction phenomenon of  $\text{CO}_2$  occurring over the photocatalyst and not from any other sources. Further, to identify the oxidative species of isopropanol (IPA) generated during photocatalysis, we utilized  $^1\text{H}$  nuclear magnetic resonance (NMR) spectroscopy technique. The analysis revealed the presence of the characteristic peak near 1.3 ppm which can be attributed to the presence of acetone, as shown in Fig. S10, which is consistent with previous reports of acetone formation as an oxidative product of IPA under similar reaction conditions. These results indicate that the  $\text{Cu-Cs}_2\text{AgBiCl}_6$  perovskite material has the potential to be an effective catalyst in the photocatalytic  $\text{CO}_2$  reduction process. Moreover, the

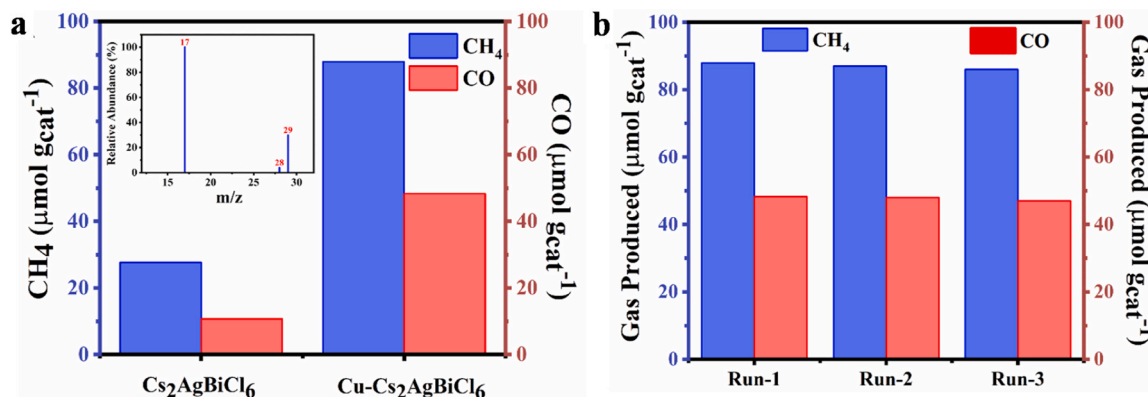


**Fig. 5.** Comparison of the photocatalytic  $\text{CO}_2$  reduction performance of the as-prepared  $\text{Cs}_2\text{AgBiCl}_6$  and  $\text{Cu-Cs}_2\text{AgBiCl}_6$  towards (a)  $\text{CH}_4$  and CO generation with inset depicting the GC-MS spectra of the labelled  $^{13}\text{CO}_2$  Photoreaction (b) Recyclability tests of the  $\text{Cu-Cs}_2\text{AgBiCl}_6$  photocatalyst toward  $\text{CO}_2$  reduction performance.

results of the cyclic tests, presented in Fig. 5B, show that the formation of CO and CH<sub>4</sub> remains relatively constant up to three cycles of photo-reduction reaction. To evaluate the stability of the Cu-Cs<sub>2</sub>AgBiCl<sub>6</sub> photocatalyst phases after the photoreaction, X-ray diffraction (XRD) analysis of the material after the photocatalysis cycles is evaluated (Fig. S11). The results demonstrate that the material remained stable and retained its initial crystal structure after the photocatalytic reaction. However, it is observed that the Cu-Cs<sub>2</sub>AgBiCl<sub>6</sub> catalyst material began to turn black beyond 14 h of irradiation, indicating potential stability issues in the structure suggesting that Cu-Cs<sub>2</sub>AgBiCl<sub>6</sub> possesses moderate stability and ways to enhance its stability can be further investigated.

### 3.5. DFT calculations

To evaluate the feasibility of Cu substitutional/interstitial doping in the Cs<sub>2</sub>AgBiCl<sub>6</sub> lattice, we calculated the formation energy ( $E_f$ ) of Cu-doped Cs<sub>2</sub>AgBiCl<sub>6</sub> with substitutional/interstitial doping using the following relation:

$$E_f = (E_{\text{Cu-Cs}_2\text{AgBiCl}_6}) - (E_{\text{Cs}_2\text{AgBiCl}_6} + \mu_{\text{Cu}})$$

Where,  $\mu_M$  and  $E_M$  represents the chemical potential and energy of corresponding components and in the case of substitutional doping we include the  $\mu_{\text{Ag}}$  in the left term. The formation energy of Cu at the Ag site was found to be  $-0.41045$  eV, lower than that of Cu at the Bi site ( $0.75$  eV) (Figs. 6a and 6b). Consequently, Cu dopants are more likely to occupy the Ag site rather than the Bi site. Additionally, no significant lattice distortion was observed in the perovskite Cs<sub>2</sub>AgBiCl<sub>6</sub> following Cu substitution at the Ag site, due to the minimal difference between the ionic radius of the two components. We also thought about the possibility of interstitial doping of Cu as its ionic radius is small in comparison to Ag<sup>+</sup> and Bi<sup>3+</sup>. Therefore, we investigated the tendency for copper to incorporate into the lattice without replacing any existing species, particularly over the center of Chlorines (Fig. 6c). The calculated formation energies revealed a value of  $-0.90$  eV, indicating a high likelihood for copper to occupy the center space of Cl atoms and reside over the Cs atom. Our experimental evidence as a negative shift in XRD pattern, elemental analysis, further supports this finding, demonstrating the incorporation of copper into the halide perovskite matrix without replacing any of the matrix's other atomic species. However, a small change was observed in the bond lengths after Cu doping due to change in local environment and enhanced coulombic interaction (Fig. S12). The surface work function is a critical parameter for characterizing the electronic properties of a material's surface. In this study, we investigated the work functions of both pristine Cs<sub>2</sub>AgBiCl<sub>6</sub> and Cu-Cs<sub>2</sub>AgBiCl<sub>6</sub> using computational methods, as illustrated in Fig. S13. The calculated work function values were determined to be  $4.95$  eV for pristine Cs<sub>2</sub>AgBiCl<sub>6</sub>,  $4.81$  and  $4.52$  eV for substitutional and interstitial Cu-Cs<sub>2</sub>AgBiCl<sub>6</sub> (111) surfaces. These results suggest that the incorporation of copper dopants elevates the Fermi level of Cs<sub>2</sub>AgBiCl<sub>6</sub>, leading to the formation of defect state energy levels near the band edges. Cs<sub>2</sub>AgBiCl<sub>6</sub> is a known p-type semiconductor; however, the introduction of interstitial Cu atoms into the crystal lattice implies that the Cu-Cs<sub>2</sub>AgBiCl<sub>6</sub> exhibits enhancement in the n-type characteristics which is in agreement with the observed UPS results. For the case of interstitial doping the increment in the n-type characteristics for Cs<sub>2</sub>AgBiCl<sub>6</sub> is more pronounced as depicted by enhanced -d-energy state contributions thus shifting the fermi levels. This effect is expected to promote the separation of photogenerated carriers and thereby enhance the material's photocatalytic activity. While our experimental observations and theoretical calculations strongly suggest the interstitial doping of copper in the Cs<sub>2</sub>AgBiCl<sub>6</sub> lattice, the impact of this doping on the material's electronic behavior necessitates detailed exploration.

Further, we have calculated the Density of States (DOS) for all three cases (Fig. 6d-f). In Cs<sub>2</sub>AgBiCl<sub>6</sub>, the valence band maximum (VBM) is predominantly composed of Cl 3p orbitals, while the case of Cu-doped

Cs<sub>2</sub>AgBiCl<sub>6</sub> PDOS reveals that copper doping introduces additional energy levels near the valance band edge (Figs. 6d and 6f). The VBM now comprises a hybrid of Ag 4d and Cu 3d orbitals (Fig. 6f). This suggests that the availability of d orbitals near the valence band, which means they can easily engage in chemical bonding with other species, making electron transfer more efficient [68,69]. This is vital in catalysis, where electron transfer is a crucial part of the process of photocatalytic reactions. It is evident near the Fermi levels that the incorporation of copper enhances the d-band energy states. We observed the shift in the d-band center (from  $-2.41$  eV to  $-4.43$  eV) (calculation details in SI-methods) upon incorporating copper into the perovskite lattice (Figs. 6d and 6f). This shift in the d-band center can have significant implications for the catalytic ability of the material [68,69]. The d-band center plays a crucial role in determining the catalytic properties of a transition metal system. A well-positioned d-band center enhances the balance between adsorption strength and desorption, which is vital for efficient catalytic activity. The energetic position of the d-states in transition metals exerts a profound influence on the strength of chemical bonding between the metal and adsorbate molecules. Specifically, an elevation in the energy of the d-states results in an increase in the energy of the antibonding (d-σ)\* states, culminating in a strengthened bond between the metal and the adsorbate. This arises from the reduction in electron occupancy of the higher-energy antibonding states, which imparts stability to the metal-adsorbate system and intensifies the binding between the two. Consequently, a higher d-band center generally confers greater bonding strength in the context of molecular chemisorption onto a metal surface. This theoretical construct has been employed with success in multiple investigations to elucidate trends in adsorption energy on transition metals. Moreover, the shift in the d-band center also indicates that the hybridization between the Ag 4d and Cu 3d orbitals in the conduction band has been altered. This change in hybridization can increase charge transfer between the metal atoms and adsorbates, further promoting the mobility of photogenerated carriers. Thus, the enhanced charge transfer and carrier mobility can significantly contribute to the material's photocatalytic ability.

The systematic investigation of the binding energy of CO<sub>2</sub> on the (111) surface of both copper-doped and undoped Cs<sub>2</sub>AgBiCl<sub>6</sub> structures was carried out. A variety of adsorption configurations were considered, both horizontal and vertical, as depicted in Fig. S14. The binding energies were evaluated over various metallic sites within the perovskite matrix, including both the native silver (Ag) sites and the newly introduced copper (Cu) sites. The findings reveal that among the multitude of adsorption sites, the most stable involved the negatively charged oxygen (O) atoms interacting with the positively charged surface metal ions (Cs-Ag). With the incorporation of copper into the structure, new positively charged Cu metal ions became available, making the adsorption more feasible at these Cu-Ag sites. Intriguingly, in addition to the newly introduced Cu sites, the Cs-Ag adsorption sites near Cu exhibited an enhanced adsorption of the CO<sub>2</sub> molecule. These nearby Cs-Ag sites behaved differently from the distant Cs-Ag sites, termed here as Cs-Ag<sub>far</sub>. The behavior of the Cs-Ag<sub>near</sub> sites also varied from those found in the undoped Cs<sub>2</sub>AgBiCl<sub>6</sub>. We also examined the binding mechanisms of the prominent intermediates, HOCO\* and CO (with detailed reaction mechanisms provided in the [Supplementary Information](#)). Observations indicate that, in addition to CO<sub>2</sub>, all intermediates were significantly more stable on Cu-Cs<sub>2</sub>AgBiCl<sub>6</sub> (as shown in Fig. S15b). Fig. S15a presents the binding mode of the HOCO\* intermediate on both Cs<sub>2</sub>AgBiCl<sub>6</sub> and Cu-Cs<sub>2</sub>AgBiCl<sub>6</sub> surfaces, emphasizing the crucial role of copper in activating the CO<sub>2</sub> reduction process. Fig. S15b also illustrates the potential energy surface for CO formation from CO<sub>2</sub> over both Cu-Cs<sub>2</sub>AgBiCl<sub>6</sub> and pristine Cs<sub>2</sub>AgBiCl<sub>6</sub> catalysts. All intermediates were significantly stabilized on the copper-doped surface, underscoring the enhanced catalytic properties imparted by copper doping. The improved binding energies upon copper doping suggest that the material exhibits a higher affinity for CO<sub>2</sub> activation, which can be beneficial for catalytic processes such as CO<sub>2</sub> reduction and other related reactions. This

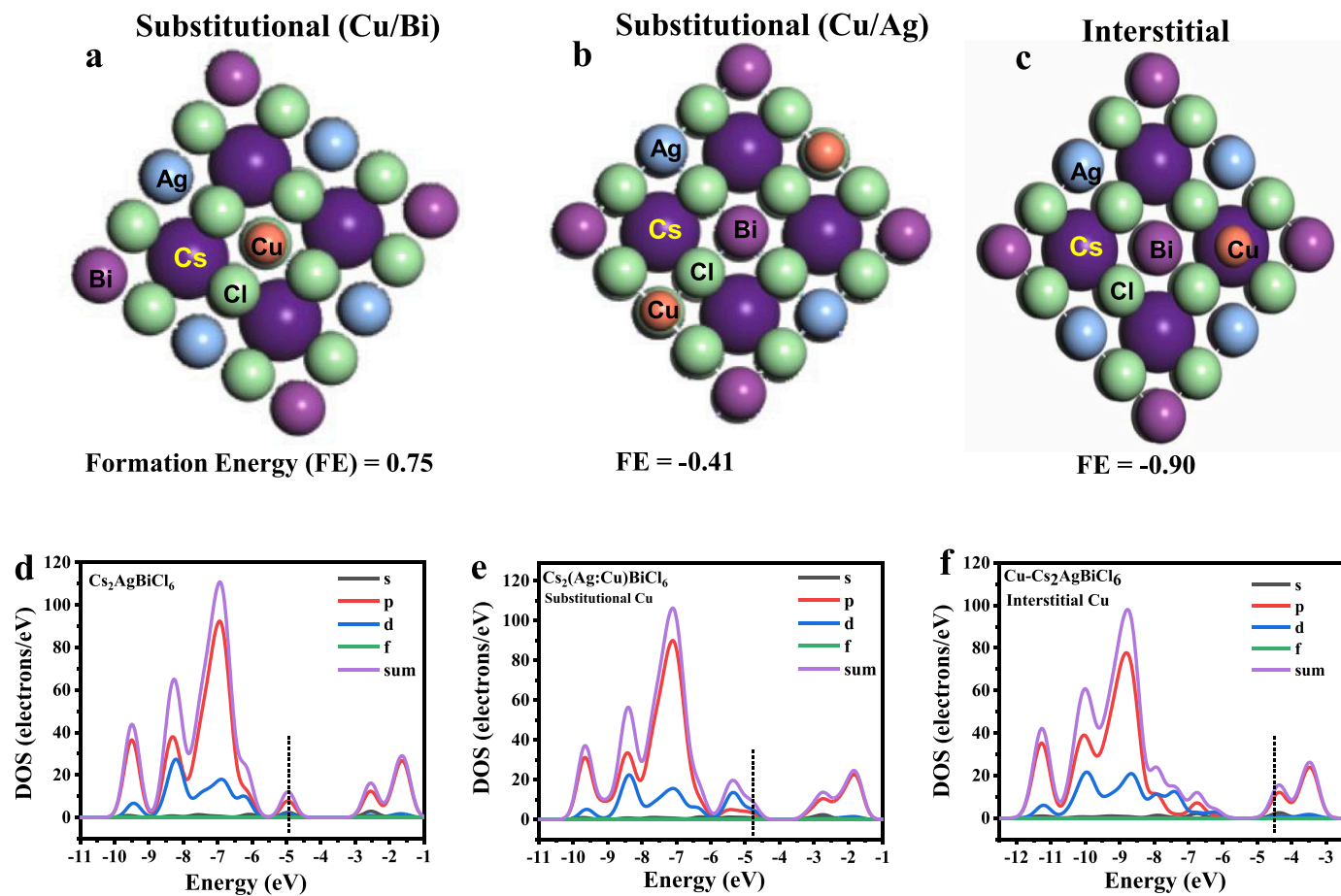


Fig. 6. (a-c) Calculated formation energies for and (d-f) density of states (DOS) plot for  $\text{Cs}_2\text{AgBiCl}_6$  and Copper doped  $\text{Cs}_2\text{AgBiCl}_6$  with substitutional and interstitial doping.



enhancement in CO<sub>2</sub> activation propensity may be attributed to the modified electronic properties of the Cu-Cs<sub>2</sub>AgBiCl<sub>6</sub>, including the shifts in the d-band center, work function, and the presence of additional energy levels near the band edges. The changes in electronic structure can facilitate the adsorption, activation, and subsequent transformation of CO<sub>2</sub> on the catalyst surface, ultimately leading to improved catalytic performance for CO<sub>2</sub> conversion processes.

### 3.6. Transient absorption measurement

As discussed above, Cu dopants were found to significantly enhance the catalytic activity of Cu-Cs<sub>2</sub>AgBiCl<sub>6</sub> in comparison to pristine Cs<sub>2</sub>AgBiCl<sub>6</sub>. To understand the influence of Cu on the photoelectrical properties of Cs<sub>2</sub>AgBiCl<sub>6</sub> and its carrier dynamics, we employed femto-second transient absorption spectroscopy, which is a useful technique for examining the optoelectronic properties, recombination dynamics, and carrier trapping mechanisms of halide perovskites. We performed the transient absorption measurement using 350 nm excitation wavelength and a broadband probe pulse with a time delay of up to 5 ns. The obtained spectrum for the Cs<sub>2</sub>AgBiCl<sub>6</sub> and Cu-Cs<sub>2</sub>AgBiCl<sub>6</sub> crystals is presented in Figs. 7a and 7b. We observed a positive peak ( $\Delta A > 0$ ) within the 480–800 nm range, which corresponds to photoinduced absorption (PIA). Typically, a positive absorption below the bandedge is indicative of self-trapped states (STSs) [22,70]. We found the motion trajectories of the PIA signal decay curves are similar for different probe wavelengths (Fig. S16), consistent with STS characteristics. The initial PIA decay was slower in Cu-Cs<sub>2</sub>AgBiCl<sub>6</sub>, as shown in the early time spectra (Fig. S16). The PIA kinetics throughout the probe wavelength

range developed within  $\sim 400$  fs - 500 fs, which is longer than the time resolution of the measurement ( $\sim 150$  fs). The fast formation time of PIA kinetics suggests no potential barrier between free excitons and carriers in STSs [71,72].

To understand the excited state dynamics and their effect on CO<sub>2</sub> reduction, we have fitted the kinetics at different probe wavelengths using a triexponential decay model in both systems (Figs. 7c, 7d, S17) and the obtained time constants are presented in Table 1. The TA kinetics in the range of 480–800 nm exhibit similar kind of decay kinetics as shown in Fig. S16 and S17. We find that all components follow the same manner in each case (without and with doping). Our observations

**Table 1**

Estimated time constants from TA kinetics using tri-exponential model for both Cs<sub>2</sub>AgBiCl<sub>6</sub> and Cu-Cs<sub>2</sub>AgBiCl<sub>6</sub> crystals.

Crystal	Band (nm)	A <sub>1</sub>	$\tau_1$ (ps)	A <sub>2</sub>	$\tau_2$ (ps)	A <sub>3</sub>	$\tau_3$ (ps)
Cs <sub>2</sub> AgBiCl <sub>6</sub>	485	0.36	3.8	0.48	144	0.16	1460
Cu-Cs <sub>2</sub> AgBiCl <sub>6</sub>	498	0.35	21.5	0.46	288	0.19	> 3000
Cs <sub>2</sub> AgBiCl <sub>6</sub>	600	0.20	6.43	0.63	177	0.17	2570
Cu-Cs <sub>2</sub> AgBiCl <sub>6</sub>	603	0.34	48.7	0.42	345	0.24	> 3000
Cs <sub>2</sub> AgBiCl <sub>6</sub>	640	0.32	5.7	0.53	135	0.15	2110
Cu-Cs <sub>2</sub> AgBiCl <sub>6</sub>	650	0.32	18.4	0.46	247	0.22	> 3000
Cs <sub>2</sub> AgBiCl <sub>6</sub>	755	0.14	3.66	0.71	66.3	0.15	1280
Cu-Cs <sub>2</sub> AgBiCl <sub>6</sub>	760	0.38	40.7	0.40	351	0.22	> 3000

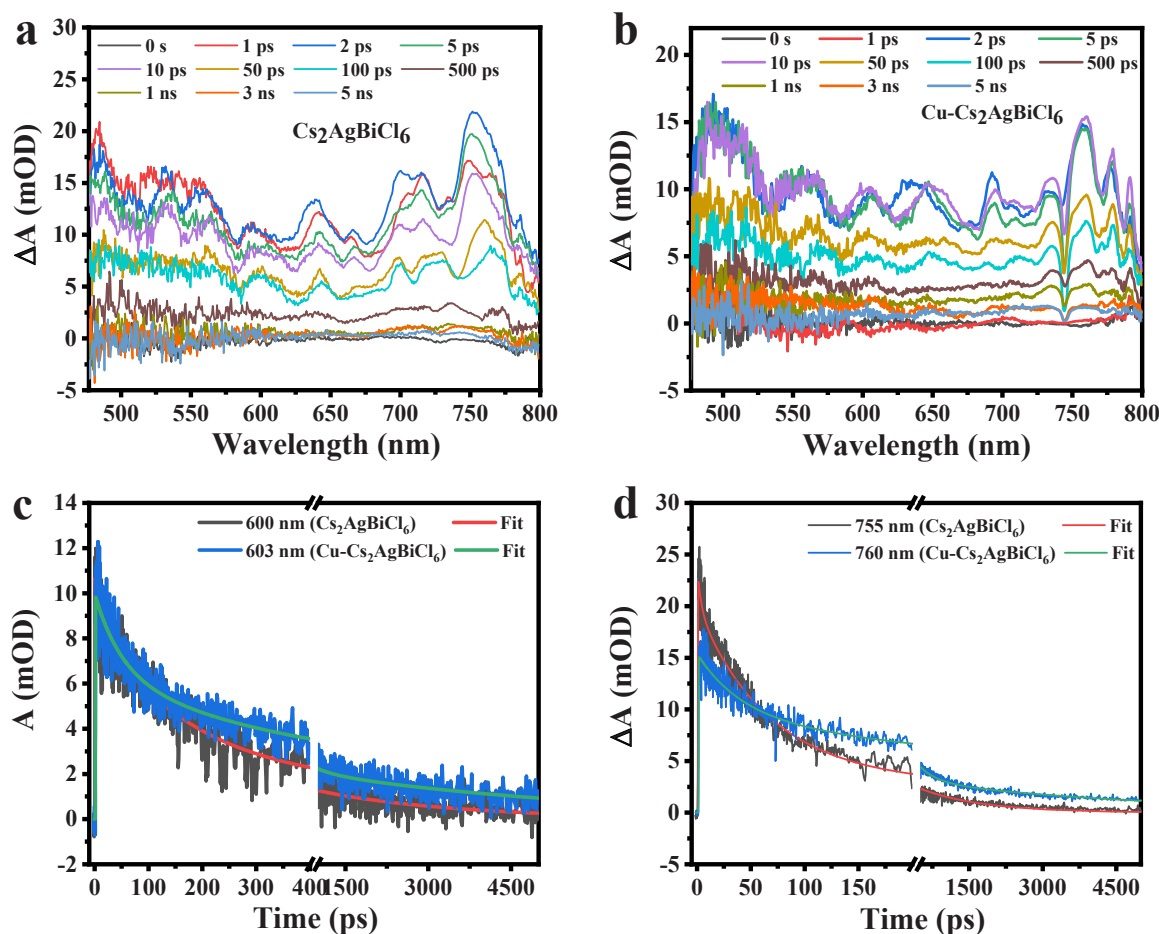


**Fig. 7.** Femtosecond transient absorption (fs-TA) spectra in response to 350 nm optical excitation of (a) Cs<sub>2</sub>AgBiCl<sub>6</sub>, and (b) Cu-Cs<sub>2</sub>AgBiCl<sub>6</sub> single crystal. Fitted kinetics monitored at (c) 600 nm for Cs<sub>2</sub>AgBiCl<sub>6</sub> and 603 nm for Cu-Cs<sub>2</sub>AgBiCl<sub>6</sub> crystal, (d) 755 nm for Cs<sub>2</sub>AgBiCl<sub>6</sub> and 760 nm for Cu-Cs<sub>2</sub>AgBiCl<sub>6</sub> crystal.

revealed that all three lifetime components were enhanced in the Cu-Cs<sub>2</sub>AgBiCl<sub>6</sub> crystal. The first component,  $\tau_1$ , is attributed to hot carrier relaxation. When a polar semiconductor is excited well above the band gap, the initial polarization dephases within femtosecond time scales, producing hot carriers. Initially, these hot excitations are delocalized, but over time, they become increasingly correlated and localized to excitonic "puddles" [29,73]. Our results showed that the hot carrier relaxation was slower in Cu-Cs<sub>2</sub>AgBiCl<sub>6</sub>, which can be attributed to the hybridization of the CBM orbitals with the copper dopants. The slow hot carrier relaxation can increase the extraction of carriers from excited states, thereby boosting CO<sub>2</sub> reduction performance. Previously, this fact was

mentioned in the case of hot carrier solar cells [74,75]. The second lifetime component  $\tau_2$  corresponds to the carrier trapping in self-trapped states. The incorporation of copper enhances the D-band energy states and elevates the Fermi level, which increases the self-trapping time of the carrier and results in more separation of carriers in Cu-Cs<sub>2</sub>AgBiCl<sub>6</sub>. The third time constant,  $\tau_3$ , corresponds to the relaxation of carriers from self-trapped states. However, it was estimated to be > 3 ns for all probe wavelengths. It should be noted that the PIA signal did not fully decay within the time window studied, and thus the accuracy of the third time constant ( $\tau_3$ ) could not be confirmed. The amplitude of the third component was found to be higher in Cu-Cs<sub>2</sub>AgBiCl<sub>6</sub>, indicating a longer carrier decay time. This suggests that the addition of copper dopants suppresses the recombination of photogenerated electrons and holes in the system. The schematic illustration of carrier dynamics in Cs<sub>2</sub>AgBiCl<sub>6</sub> and Cu-Cs<sub>2</sub>AgBiCl<sub>6</sub> is presented in Fig. S18.

With all experiments and theoretical calculations, we found that the interstitial Cu dopants in Cs<sub>2</sub>AgBiCl<sub>6</sub> provide more sites for CO<sub>2</sub> adsorption and activation. These new adsorption sites exhibit a stronger interaction with CO<sub>2</sub> molecules, promoting CO<sub>2</sub> activation and dissociation. The enhanced absorption of CO and the stronger interaction between CO and the active sites may contribute to the higher selectivity of CH<sub>4</sub> for Cu-Cs<sub>2</sub>AgBiCl<sub>6</sub>. The introduction of copper dopants creates new energy levels within the bandgap of Cs<sub>2</sub>AgBiCl<sub>6</sub>, leading to an augmented charge separation efficiency and promoting the formation of active sites crucial for CO<sub>2</sub> reduction. Previously, it was reported that Cu introduces sub-bandgap defects, which enhances the photoconductivity due to strong sub-bandgap absorption leading to appreciable photo-carrier generation. The introduction of Cu ions into the lattice results in improved separation and reduced recombination of carriers, which is a crucial factor in determining the photocatalytic activity of the material. The localized electronic states of Cu<sup>+</sup> possess donor-acceptor properties, which facilitate the dissociation of excitons confined to the octahedra via Cu 4s and 3d orbitals, resulting in enhanced extraction of excited carriers. Therefore, Cu-Cs<sub>2</sub>AgBiCl<sub>6</sub> produces more photoexcited carriers that actively engage in surface reactions. This substantial increase in photoexcited carriers directly contributes to the enhanced catalytic activity observed for CO<sub>2</sub> reduction.

#### 4. Conclusions

In conclusion, we have demonstrated that Cu-doping significantly enhances the photocatalytic CO<sub>2</sub> reduction performance of Cs<sub>2</sub>AgBiCl<sub>6</sub> perovskite. The introduction of Cu-doping into Cs<sub>2</sub>AgBiCl<sub>6</sub> perovskite crystals has been shown to significantly enhance light absorption by introducing active energy sites between the energy bands. Cu-Cs<sub>2</sub>AgBiCl<sub>6</sub> perovskite has demonstrated remarkable activity in CO<sub>2</sub> photo-reduction, achieving 88 and 48  $\mu\text{mol/g}_{\text{cat}}$  for CH<sub>4</sub> and CO products, respectively, which are both higher than those of pristine Cs<sub>2</sub>AgBiCl<sub>6</sub> (27 and 10  $\mu\text{mol/g}_{\text{cat}}$ ). Experiments and theoretical calculations show that Cu incorporated as interstitial dopants in Cs<sub>2</sub>AgBiCl<sub>6</sub> and modulate the Fermi level by enhancing the d-band energy states, which facilitate the dissociation of excitons and suppress carrier recombination in Cu-Cs<sub>2</sub>AgBiCl<sub>6</sub>, leading to more carriers participating in surface catalytic reactions. Transient absorption results indicate that hot carrier

relaxation is slower, and carrier decay lifetime is extended in Cu-Cs<sub>2</sub>AgBiCl<sub>6</sub>, enhancing charge migration efficiency, and boosting CO<sub>2</sub> reduction performance. These findings provide valuable insights into the mechanism of CO<sub>2</sub> reduction in Cu-doped Cs<sub>2</sub>AgBiCl<sub>6</sub> perovskite crystals and suggest that Cu-doping is a promising strategy for developing highly efficient CO<sub>2</sub> reduction photocatalysts. Future research could explore further optimization of the Cu-doping concentration and investigate the stability of perovskite crystals under different reaction conditions.

#### CRedit authorship contribution statement

**Naveen Kumar Tailor:** Investigation, Formal analysis, Writing – original draft. **Shreya Singh:** Investigation, Formal analysis, Writing – original draft. **Mohammad Adil Afroz:** Formal analysis, Writing – review & editing. **Kamal Kishore Pant:** Validation, Formal analysis, Writing – review & editing, Supervision, Project administration. **Soumitra Satapathi:** Conceptualization, Methodology, Validation, Formal analysis, Writing – review & editing, Supervision, Project administration, Funding acquisition.

#### Declaration of Competing Interest

The authors declare that they have no known competing financial interests or personal relationships that could have appeared to influence the work reported in this paper.

#### Data Availability

Data will be made available on request.

#### Acknowledgments

NKT acknowledges the grant SER-1852-PHY. SS acknowledges PMRF fellowship and HPC IIT Delhi. KKP like to acknowledge DST, Government of India under Technology Mission Division (Sanction no. TM/EWO/MICCUS/19C). SS like to acknowledge SERB IRPHA Grant (IPA/2021/000096).

#### Supporting Information

Supporting Information is available free of charge.

EDXA spectra and elemental analysis table of Cs<sub>2</sub>AgBiCl<sub>6</sub> and Cu-Cs<sub>2</sub>AgBiCl<sub>6</sub>, ICPMS results, XRD pattern of Cs<sub>2</sub>AgBiCl<sub>6</sub> and Cu-Cs<sub>2</sub>AgBiCl<sub>6</sub> powder, FWHM, crystallite size, lattice strain of prominent plane, Fitted XPS spectra, room temperature EPR spectrum, band levels, CO<sub>2</sub> temperature programmed desorption profile for Cu-Cs<sub>2</sub>AgBiCl<sub>6</sub> photocatalyst, H NMR spectra for the liquid product obtained after the CO<sub>2</sub> photoreduction reaction, XRD spectra after the photoreduction reaction experiment, calculated bond lengths, bandgaps, and work-Function, Adsorption configurations of CO<sub>2</sub>, binding mode of HOCO\*-intermediate, TA spectra in early time upto 100 ps and rise kinetics, fitted TA kinetics, schematic illustration of carrier dynamics.

#### Appendix A. Supporting information

Supplementary data associated with this article can be found in the online version at doi:10.1016/j.apcatb.2023.123247.

#### References

- [1] J. Artz, T.E. Muller, K. Thenert, J. Kleinekorte, R. Meys, A. Sternberg, A. Bardow, W. Leitner, Sustainable conversion of carbon dioxide: an integrated review of catalysis and life cycle assessment, *Chem. Rev.* 118 (2018) 434–504.
- [2] S. Chu, Y. Cui, N. Liu, The path towards sustainable energy, *Nat. Mater.* 16 (2016) 16–22.

- [3] J.C. Osorio-Aravena, A. Aghahosseini, D. Bogdanov, U. Caldera, N. Ghorbani, T.N. O. Mensah, S. Khalili, E. Munoz-Ceron, C. Breyer, The impact of renewable energy and sector coupling on the pathway towards a sustainable energy system in Chile, *Renew. Sustain. Energy Rev.* 151 (2021), 111557.
- [4] Q.W. Song, Z.H. Zhou, L.N. He, Efficient, selective and sustainable catalysis of carbon dioxide, *Green. Chem.* 19 (2017) 3707–3728.
- [5] T. Inoue, A. Fujishima, S. Konishi, K. Honda, Photoelectrocatalytic reduction of carbon-dioxide in aqueous suspensions of semiconductor powders, *Nature* 277 (1979) 637–638.
- [6] X. Chen, R.T. Guo, L.F. Hong, Y. Yuan, W.G. Pan, Research progress on CO<sub>2</sub> photocatalytic reduction with full solar spectral responses, *Energy Fuels* 35 (2021) 19920–19942.
- [7] A.D. Handoko, K.F. Li, J.W. Tang, Recent progress in artificial photosynthesis: CO<sub>2</sub> photoreduction to valuable chemicals in a heterogeneous system, *Curr. Opin. Chem. Eng.* 2 (2013) 200–206.
- [8] M.A. Hossen, H.M. Solayman, K.H. Leong, L.C. Sim, N. Yaacof, A. Abd Aziz, L. Wu, M.U. Monir, Recent progress in TiO<sub>2</sub>-Based photocatalysts for conversion of CO<sub>2</sub> to hydrocarbon fuels: a systematic review, *Results Eng.* 16 (2022), 100795.
- [9] X. Li, S. Wang, L. Li, Y. Sun, Y. Xie, Progress and perspective for in situ studies of CO(2) reduction, *J. Am. Chem. Soc.* 142 (2020) 9567–9581.
- [10] X. Yang, K. Li, G. Wang, X. Li, P. Zhou, S. Ding, Z. Lyu, Y.C. Chang, Y. Zhou, W. Zhu, 2D catalysts for CO(2) photoreduction: discussing structure efficiency strategies and prospects for scaled production based on current progress, *Chemistry* 28 (2022), e202201881.
- [11] J.Q. Luo, W.W. Zhang, H.B. Yang, Q.W. Fan, F.Q. Xiong, S.J. Liu, D.S. Li, B. Liu, Halide perovskite composites for photocatalysis: a mini review, *Ecomat* 3 (2021), e12079.
- [12] K. Ren, S. Yue, C. Li, Z. Fang, K.A.M. Gasem, J. Leszczynski, S. Qu, Z. Wang, M. Fan, Metal halide perovskites for photocatalysis applications, *J. Mater. Chem. A* 10 (2022) 407–429.
- [13] S. Singh, A. Modak, K.K. Pant, CO<sub>2</sub> reduction to methanol using a conjugated organic-inorganic hybrid TiO<sub>2</sub>-C<sub>3</sub>N<sub>4</sub> nano-assembly, *Trans. Indian Natl. Acad. Eng.* 6 (2021) 395–404.
- [14] S. Singh, A. Modak, K.K. Pant, A. Sinhamahapatra, P. Biswas, MoS<sub>2</sub>-nanosheets-based catalysts for photocatalytic CO<sub>2</sub> reduction: a review, *ACS Appl. Nano Mater.* 4 (2021) 8644–8667.
- [15] S. Singh, R. Punia, K.K. Pant, P. Biswas, Effect of work-function and morphology of heterostructure components on CO<sub>2</sub> reduction photo-catalytic activity of MoS<sub>2</sub>-Cu<sub>2</sub>O heterostructure, *Chem. Eng. J.* 433 (2022), 132709.
- [16] J. Chen, C. Dong, H. Idriss, O.F. Mohammed, O.M. Bakr, Metal halide perovskites for solar-to-chemical fuel conversion, *Adv. Energy Mater.* 10 (2019) 1902433.
- [17] Z. Zhang, Y. Jiang, M. Shu, L. Li, Z. Dong, J. Xu, Artificial photosynthesis over metal halide perovskites: achievements, challenges, and prospects, *J. Phys. Chem. Lett.* 12 (2021) 5864–5870.
- [18] Z.C. Kong, J.F. Liao, Y.J. Dong, Y.F. Xu, H.Y. Chen, D.B. Kuang, C.Y. Su, Core@Shell CsPbBr<sub>3</sub>@zeolitic imidazolate framework nanocomposite for efficient photocatalytic CO<sub>2</sub> reduction, *ACS Energy Lett.* 3 (2018) 2656–2662.
- [19] Y.F. Xu, M.Z. Yang, B.X. Chen, X.D. Wang, H.Y. Chen, D.B. Kuang, C.Y. Su, A. CsPbBr<sub>3</sub> Perovskite quantum dot/graphene oxide composite for photocatalytic CO(2) reduction, *J. Am. Chem. Soc.* 139 (2017) 5660–5663.
- [20] N.K. Tailor, S. Kar, P. Mishra, A. These, C. Kupfer, H.L. Hu, M. Awais, M. Saidaminov, M.I. Dar, C. Brabec, S. Satapathi, Advances in lead-free perovskite single crystals: fundamentals and applications, *ACS Mater. Lett.* 3 (2021) 1025–1080.
- [21] N.K. Tailor, N. Parikh, P. Yadav, S. Satapathi, Dielectric relaxation and polaron hopping in Cs<sub>2</sub>AgBiBr<sub>6</sub> halide double perovskites, *J. Phys. Chem. C* 126 (2022) 10199–10208.
- [22] N.K. Tailor, S.K. Saini, P. Yadav, M. Kumar, S. Satapathi, Elucidating polaron dynamics in Cs(2)AgBiBr(6) double perovskite, *J. Phys. Chem. Lett.* 14 (2023) 730–736.
- [23] N.K. Tailor, S. Satapathi, The impact of Cs<sub>3</sub>Bi<sub>2</sub>Cl<sub>9</sub> single crystal growth modality on its symmetry and morphology, *J. Mater. Res. Technol.* 9 (2020) 7149–7157.
- [24] N.K. Tailor, J. Ghosh, M.A. Afroz, J. Bennett, M. Chatterjee, P. Sellin, S. Satapathi, Self-powered X-ray detection and imaging using Cs<sub>2</sub>AgBiCl<sub>6</sub> lead-free double perovskite single crystal, *ACS Appl. Electron. Mater.* 4 (2022) 4530–4539.
- [25] M. Miodynska, T. Klimczuk, W. Lisowski, A. Zaleska-Medynska, Bi-based halide perovskites: Stability and opportunities in the photocatalytic approach for hydrogen evolution, *Catal. Commun.* 177 (2023), 106656.
- [26] L. Ding, Y. Ding, F. Bai, G. Chen, S. Zhang, X. Yang, H. Li, X. Wang, In situ growth of Cs(3)Bi(2)Br(9) quantum dots on Bi-MOF nanosheets via cosharing bismuth atoms for CO(2) capture and photocatalytic reduction, *Inorg. Chem.* 62 (2023) 2289–2303.
- [27] L. Wu, S. Zheng, H. Lin, S. Zhou, A. Mahmoud Idris, J. Wang, S. Li, Z. Li, In-situ assembling 0D/2D Z-scheme heterojunction of Lead-free Cs(2)AgBiBr(6)/Bi(2)WO(6) for enhanced photocatalytic CO(2) reduction, *J. Colloid Interface Sci.* 629 (2023) 233–242.
- [28] Y. Feng, D. Chen, Y. Zhong, Z. He, S. Ma, H. Ding, W. Ao, X. Wu, M. Niu, A. Lead-Free, 0D/2D Cs(3)Bi(2)Br(9)/Bi(2)WO(6) S-scheme heterojunction for efficient photoreduction of CO(2), *ACS Appl. Mater. Interfaces* 15 (2023) 9221–9230.
- [29] N.K. Tailor, S. Mishra, T. Sharma, A.K. De, S. Satapathi, Cation-dependent hot carrier cooling in the lead-free bismuth halide A<sub>3</sub>Bi<sub>2</sub>I<sub>9</sub> (A = FA, MA, and Cs) perovskite, *J. Phys. Chem. C* 125 (2021) 9891–9898.
- [30] N.K. Tailor, S. Satapathi, Crystalline-liquid duality of specific heat in halide perovskite semiconductor, *Scr. Mater.* 223 (2023), 115061.
- [31] N.K. Tailor, A. Listorti, S. Colella, S. Satapathi, Lead-free halide double perovskites: fundamentals, challenges, and photovoltaics applications, *Adv. Mater. Technol.* 8 (2022) 2200442.
- [32] N.K. Tailor, S. Satapathi, Photosensitive dielectric and conductivity relaxation in lead-free Cs<sub>3</sub>Bi<sub>2</sub>Cl<sub>9</sub> perovskite single crystals, *J. Phys. Chem. C* 125 (2021) 5243–5250.
- [33] N.K. Tailor, S. Satapathi, Structural disorder and spin dynamics study in millimeter-sized all-inorganic lead-free cesium bismuth halide perovskite single crystals, *ACS Appl. Energy Mater.* 3 (2020) 11732–11740.
- [34] D.F. Wu, X.S. Zhao, Y.Y. Huang, J.N. Lai, J.Y. Yang, C.Q. Tian, P. He, Q. Huang, X. S. Tang, Synthesis and CO<sub>2</sub> photoreduction of lead-free cesium bismuth halide perovskite nanocrystals, *J. Phys. Chem. C* 125 (2021) 18328–18333.
- [35] J. Pi, X. Jia, Z. Long, S. Yang, H. Wu, D. Zhou, Q. Wang, H. Zheng, Y. Yang, J. Zhang, J. Qiu, Surface and defect engineering coupling of halide double perovskite Cs<sub>2</sub>NaBiCl<sub>6</sub> for efficient CO<sub>2</sub> photoreduction, *Adv. Energy Mater.* 12 (2022) 2202074.
- [36] M.S. Sena, J.Y. Cui, Y. Baghdadi, E. Rattner, M. Daboczi, A.L. Lopes-Moriyama, A. G. dos Santos, S. Eslava, Lead-free halide perovskite Cs<sub>2</sub>AgBiBr<sub>6</sub>/bismuthene composites for improved CH<sub>4</sub> production in photocatalytic CO<sub>2</sub> reduction, *ACS Appl. Energy Mater.* (2023).
- [37] S. Kumar, I. Hassan, M. Regue, S. Gonzalez-Carrero, E. Rattner, M.A. Isaacs, S. Eslava, Mechanochemically synthesized Pb-free halide perovskite-based Cs<sub>2</sub>AgBiBr<sub>6</sub>-Cu-RGO nanocomposite for photocatalytic CO<sub>2</sub> reduction, *J. Mater. Chem. A* 9 (2021) 12179–12187.
- [38] M. Ou, W. Tu, S. Yin, W. Xing, S. Wu, H. Wang, S. Wan, Q. Zhong, R. Xu, Amino-assisted anchoring of CsPbBr<sub>3</sub> perovskite quantum dots on porous g-C(3)N(4) for enhanced photocatalytic CO(2) reduction, *Angew. Chem.* 57 (2018) 13570–13574.
- [39] H. Bian, T.F. Liu, D. Li, Z. Xu, J.H. Lian, M. Chen, J.Q. Yan, S.Z.F. Liu, Unveiling the effect of interstitial dopants on CO<sub>2</sub> activation over CsPbBr<sub>3</sub> catalyst for efficient photochemical CO<sub>2</sub> reduction, *Chem. Eng. J.* 435 (2022), 135071.
- [40] M. Shi, G. Li, W. Tian, S. Jin, X. Tao, Y. Jiang, J. Xu, NiFe-layered double hydroxides/lead-free Cs(2)AgBiBr(6) perovskite 2D/2D heterojunction for photocatalytic CO(2) conversion, *Inorg. Chem.* 62 (2023) 1752–1761.
- [42] H. Fu, X. Liu, Y. Wu, Q. Zhang, Z. Wang, Z. Zheng, H. Cheng, Y. Liu, Y. Dai, B. Huang, P. Wang, Construction of a bismuth-based perovskite direct Z-scheme heterojunction Au-Cs<sub>3</sub>Bi<sub>2</sub>Br<sub>9</sub>/V<sub>2</sub>O<sub>5</sub> for efficient photocatalytic CO<sub>2</sub> reduction, *Appl. Surface Sci.* 622 (2023) 156964.
- [43] S. Shyamal, S.K. Dutta, N. Pradhan, Doping iron in CsPbBr<sub>3</sub> perovskite nanocrystals for efficient and product selective CO(2) reduction, *J. Phys. Chem. Lett.* 10 (2019) 7965–7969.
- [44] C.C. Lin, T.R. Liu, S.R. Lin, K.M. Boopathi, C.H. Chiang, W.Y. Tzeng, W.C. Chien, H. S. Hsu, C.W. Luo, H.Y. Tsai, H.A. Chen, P.C. Kuo, J. Shiue, J.W. Chiou, W.F. Pong, C.C. Chen, C.W. Chen, Spin-polarized photocatalytic CO(2) reduction of Mn-doped perovskite nanoplates, *J. Am. Chem. Soc.* 144 (2022) 15718–15726.
- [45] X.M. Zhang, R. Tang, F. Li, R.K. Zheng, J. Huang, Tailoring inorganic halide perovskite photocatalysts toward carbon dioxide reduction, *Sol. RRL* 6 (2022) 2101058.
- [46] C. Tang, C.Y. Chen, W.W. Xu, L. Xu, Design of doped cesium lead halide perovskite as a photo-catalytic CO<sub>2</sub> reduction catalyst, *J. Mater. Chem. A* 7 (2019) 6911–6919.
- [47] Y. Liu, X. Zheng, Y. Fang, Y. Zhou, Z. Ni, X. Xiao, S. Chen, J. Huang, Ligand assisted growth of perovskite single crystals with low defect density, *Nat. Commun.* 12 (2021) 1686.
- [48] L.Q. Xie, L. Chen, Z.A. Nan, H.X. Lin, T. Wang, D.P. Zhan, J.W. Yan, B.W. Mao, Z. Q. Tian, Understanding the cubic phase stabilization and crystallization kinetics in mixed cations and halides perovskite single crystals, *J. Am. Chem. Soc.* 139 (2017) 3320–3323.
- [49] H.J. Yen, P.W. Liang, C.C. Chueh, Z. Yang, A.K. Jen, H.L. Wang, Large grained perovskite solar cells derived from single-crystal perovskite powders with enhanced ambient stability, *ACS Appl. Mater. Interfaces* 8 (2016) 14513–14520.
- [50] Y. Zhao, I. Yavuz, M. Wang, M.H. Weber, M. Xu, J.H. Lee, S. Tan, T. Huang, D. Meng, R. Wang, J. Xue, S.J. Lee, S.H. Bae, A. Zhang, S.G. Choi, Y. Yin, J. Liu, T. H. Han, Y. Shi, H. Ma, W. Yang, Q. Xing, Y. Zhou, P. Shi, S. Wang, E. Zhang, J. Bian, X. Pan, N.G. Park, J.W. Lee, Y. Yang, Suppressing ion migration in metal halide perovskite via interstitial doping with a trace amount of multivalent cations, *Nat. Mater.* 21 (2022) 1396–1402.
- [51] Y. Lin, Y. Shao, J. Dai, T. Li, Y. Liu, X. Dai, X. Xiao, Y. Deng, A. Gruverman, X. C. Zeng, J. Huang, Metallic surface doping of metal halide perovskites, *Nat. Commun.* 12 (2021) 7.
- [52] M.C. Biesinger, Advanced analysis of copper X-ray photoelectron spectra, *Surface Interface, Analysis* 49 (2017) 1325–1334.
- [53] C. Geng, S. Wang, X. Shen, Z.Q. Xu, L.T. Li, E.C. Zhao, J. Zhang, S.Y. Ma, J.H. Sun, W.Z. Wu, L.M. An, K. Pan, Enhanced charge carrier transport in lead-free double-perovskite Cs<sub>2</sub>AgBiCl<sub>6</sub> nanocrystals grown in situ on reduced graphene oxides, *J. Phys. Chem. C* 126 (2022) 1055–1063.
- [54] S. Ghosh, G.K. Nim, H. Shankar, P. Kar, Probing the emissive behaviour of the lead-free Cs<sub>2</sub>AgBiCl<sub>6</sub> double perovskite with Cu(II) doping, *New J. Chem.* 45 (2021) 22691–22696.
- [55] S. Thawarkar, S.R. Rondiya, N.Y. Dzade, N. Khupse, S. Jadkar, Experimental and theoretical investigation of the structural and opto-electronic properties of Fe-doped lead-free Cs(2) AgBiCl(6) double perovskite, *Chemistry* 27 (2021) 7408–7417.

- [56] M. Wang, P. Zeng, Z. Wang, M. Liu, Vapor-deposited Cs<sub>2</sub>AgBiCl<sub>6</sub>(6) double perovskite films toward highly selective and stable ultraviolet photodetector, *Adv. Sci.* 7 (2020) 1903662.
- [57] M. Jeevaraj, P. Devendran, N. Nallamuthu, S. Sudhahar, M.K. Kumar, Influence of Mn<sup>2+</sup> doping on the optical properties of Cs<sub>2</sub>AgBiCl<sub>6</sub> double perovskite luminescent phosphors, *J. Mater. Sci. Mater. Electron.* 34 (2023) 65.
- [58] G. Zhang, D. Wang, B. Lou, C.G. Ma, A. Meijerink, Y. Wang, Efficient broadband near-infrared emission from lead-free halide double perovskite single crystal, *Angew. Chem.* 61 (2022), e202207454.
- [59] L. Zhang, Y.Y. Fang, L.Z. Sui, J.J. Yan, K. Wang, K.J. Yuan, W.L. Mao, B. Zou, Tuning emission and electron-phonon coupling in lead-free halide double perovskite Cs<sub>2</sub>AgBiCl<sub>6</sub> under pressure, *ACS Energy Lett.* 4 (2019) 2975–2982.
- [60] B.I. Ito, E.K. Tekelenburg, G.R. Blake, M.A. Loi, A.F. Nogueira, Double perovskite single-crystal photoluminescence quenching and resurge: the role of Cu doping on its photophysics and crystal structure, *J. Phys. Chem. Lett.* 12 (2021) 10444–10449.
- [61] F. Ji, Y. Huang, F. Wang, L. Kobera, F. Xie, J. Klarbring, S. Abbrent, J. Brus, C. Yin, S.I. Simak, I.A. Abrikosov, I.A. Buyanova, W.M. Chen, F. Gao, Near-infrared light-responsive Cu-doped Cs<sub>2</sub>AgBiBr<sub>6</sub>, *Adv. Funct. Mater.* 30 (2020) 2005521.
- [62] P.K. Nayak, M. Sendner, B. Wenger, Z. Wang, K. Sharma, A.J. Ramadan, R. Lovrincic, A. Pucci, P.K. Madhu, H.J. Snaith, Impact of Bi(3+) heterovalent doping in organic-inorganic metal halide perovskite crystals, *J. Am. Chem. Soc.* 140 (2018) 574–577.
- [63] M.A. Haque, D.R. Villalva, L.H. Hernandez, R. Tounesi, S. Jang, D. Baran, Role of dopants in organic and halide perovskite energy conversion devices, *Chem. Mater.* 33 (2021) 8147–8172.
- [64] Q. Jiang, M. Chen, J. Li, M. Wang, X. Zeng, T. Besara, J. Lu, Y. Xin, X. Shan, B. Pan, C. Wang, S. Lin, T. Siegrist, Q. Xiao, Z. Yu, Electrochemical doping of halide perovskites with ion intercalation, *ACS Nano* 11 (2017) 1073–1079.
- [65] F. Zu, D. Shin, N. Koch, Electronic properties of metal halide perovskites and their interfaces: the basics, *Mater. Horiz.* 9 (2022) 17–24.
- [66] X. Liu, J. Fan, C. Huang, Advances in theoretical calculation of halide perovskites for photocatalysis, *Front. Nanotechnol.* 3 (2021), 695490.
- [67] M. Méndez-Galván, B. Alcántar-Vázquez, G. Díaz, I.A. Ibarra, H.A. Lara-García, Metal halide perovskites as an emergent catalyst for CO<sub>2</sub> photoreduction: a minireview, *React. Chem. Eng.* 6 (2021) 828–838.
- [68] M. García-Mota, A. Vojvodic, F. Abild-Pedersen, J.K. Nørskov, Electronic origin of the surface reactivity of transition-metal-doped TiO<sub>2</sub>(110), *J. Phys. Chem. C* 117 (2012) 460–465.
- [69] H.B. Tao, L. Fang, J. Chen, H.B. Yang, J. Gao, J. Miao, S. Chen, B. Liu, Identification of Surface Reactivity Descriptor for Transition Metal Oxides in Oxygen Evolution Reaction, *J. Am. Chem. Soc.* 138 (2016) 9978–9985.
- [70] N.K. Tailor, K.S. Saini, M. Kumar, S. Satapathi, Polaron-mediated photoconduction in lead-free single-crystalline perovskite thin-film devices, *J. Phys. Chem. C* 126 (2022) 11165–11173.
- [71] J. Yu, J. Kong, W. Hao, X. Guo, H. He, W.R. Leow, Z. Liu, P. Cai, G. Qian, S. Li, X. Chen, X. Chen, Broadband extrinsic self-trapped exciton emission in Sn-doped 2D lead-halide perovskites, *Adv. Mater.* 31 (2019), e1806385.
- [72] L. Zhou, J.F. Liao, Z.G. Huang, J.H. Wei, X.D. Wang, H.Y. Chen, D.B. Kuang, Intrinsic self-trapped emission in 0D lead-free C(4) H(14) N(2))(2) In(2) Br(10) single crystal, *Angew. Chem.* 58 (2019) 15435–15440.
- [73] N.K. Tailor, P. Maity, S. Satapathi, Phonon-mediated slow hot carrier dynamics in lead-free Cs<sub>3</sub>Bi(2)I(9) perovskite single crystal, *J. Phys. Chem. Lett.* (2022) 5260–5266.
- [74] S. Kahmann, M.A. Loi, Hot carrier solar cells and the potential of perovskites for breaking the Shockley-Queisser, Limit, *J. Mater. Chem. C* 7 (2019) 2471–2486.
- [75] M. Li, J. Fu, Q. Xu, T.C. Sum, Slow hot-carrier cooling in halide perovskites: prospects for hot-carrier solar cells, *Adv. Mater.* 31 (2019), e1802486.